MATERIALS SCIENCE

Supercooled liquid sulfur maintained in three-dimensional current collector for high-performance Li-S batteries

Guangmin Zhou[1,2]*, Ankun Yang[1]*, Guoping Gao[3]*, Xiaoyun Yu[1], Jinwei Xu[1], Chenwei Liu[1], Yusheng Ye[1], Allen Pei[1], Yecun Wu[1], Yucan Peng[1], Yanxi Li[1], Zheng Liang[1], Kai Liu[1], Lin-Wang Wang[3], Yi Cui[1,4]†

In lithium-sulfur (Li-S) chemistry, the electrically/ionically insulating nature of sulfur and Li_2S leads to sluggish electron/ion transfer kinetics for sulfur species conversion. Sulfur and Li_2S are recognized as solid at room temperature, and solid-liquid phase transitions are the limiting steps in Li-S batteries. Here, we visualize the distinct sulfur growth behaviors on Al, carbon, Ni current collectors and demonstrate that (i) liquid sulfur generated on Ni provides higher reversible capacity, faster kinetics, and better cycling life compared to solid sulfur; and (ii) Ni facilitates the phase transition (e.g., Li_2S decomposition). Accordingly, light-weight, 3D Ni-based current collector is designed to control the deposition and catalytic conversion of sulfur species toward high-performance Li-S batteries. This work provides insights on the critical role of the current collector in determining the physical state of sulfur and elucidates the correlation between sulfur state and battery performance, which will advance electrode designs in high-energy Li-S batteries.

INTRODUCTION

The increasing demand for high–energy density batteries has driven the development of new battery chemistries beyond the conventional lithium ion intercalation reactions (*1*). Lithium-sulfur (Li-S) batteries are regarded as next-generation high-energy storage devices for portable electronics, electric vehicles, and grid-scale storage due to their high theoretical energy density (*2*, *3*). Meanwhile, sulfur, produced as a by-product of the petroleum refining process, is naturally abundant, inexpensive, and environmentally benign (*4*). However, the insulating nature of bulk sulfur and lithium sulfide (Li_2S) leads to large polarization and sluggish reaction kinetics, requiring high activation voltages to drive the overall redox process (*5*). In addition, dissolved lithium polysulfides can be reduced at the lithium anode and diffuse back to the cathode, causing the "shuttle effect" and resulting in rapid capacity decay and low Coulombic efficiency (*6*). Therefore, the low active material utilization, low sulfur loading, inferior reaction kinetics, and poor cycling stability seriously restrict the practical application of Li-S batteries.

To address the above challenges, substantial efforts have been made to physically confine sulfur and polysulfides within the pores of carbonaceous materials (*7*–*10*) and block polysulfide diffusion through interlayers or separator modification (*11*, *12*). However, because of the weak interaction between nonpolar carbon materials and polar lithium polysulfides/Li_2S (*13*), the polysulfide shuttle effect cannot be effectively suppressed through carbon-based strategies. Therefore, polar hosts such as metal oxides (*14*), metal nitrides (*15*), metal sulfides (*16*), heteroatom-doped carbon materials (*17*, *18*), and polymers (*19*, *20*) have been introduced to chemically immobilize sulfur species and reduce the dissolution of lithium polysulfides.

In addition to the need for adsorbing and trapping lithium polysulfides, it is also well known that the accumulation of insulating sulfur species will passivate the active interface toward further redox chemistry, leading to slow sulfur-polysulfides-Li_2S conversion reaction kinetics (*21*, *22*). Therefore, controlling sulfur/Li_2S precipitation and accelerating sulfur redox reactions are critical in improving Li-S battery performance. Recent works have studied the electrocatalytic effects of metals (*23*, *24*) and metal compounds (*25*, *26*) in Li-S batteries and demonstrated accelerated sulfur conversion reactions during battery operation. However, less attention has been paid to the current collector materials (*27*–*29*), in particular about their effect on sulfur/Li_2S formation, dissolution, and precipitation, as well as the electrochemical performance of Li-S batteries (*30*, *31*). Moreover, the direct real-time observation of sulfur species evolution at the microscale and investigation of their reaction kinetics are still lacking.

Meanwhile, it is generally accepted that the solid-liquid conversion reaction, i.e., going from solid Li_2S to liquid lithium polysulfides and back or from polysulfides to solid sulfur, are the controlling steps for high rate capability in Li-S batteries (*21*, *22*). Recently, our group found an unexpected phenomenon that the charging product sulfur can remain as a liquid in a supercooled state instead of being solid in electrochemical Li-S cells at room temperature, well below its melting point (115.2°C) (*32*). This behavior brings up new opportunities to explore the Li-S battery performance with liquid sulfur and the kinetics of liquid-liquid conversion. To address these new directions, a fundamental understanding of the reaction mechanism at the electrode/electrolyte interface and corresponding electrode design for battery testing are needed.

[1]Department of Materials Science and Engineering, Stanford University, Stanford, CA 94305, USA. [2]Shenzhen Geim Graphene Center, Tsinghua-Berkeley Shenzhen Institute and Tsinghua Shenzhen International Graduate School, Tsinghua University, Shenzhen 518055, China. [3]Materials Sciences Division, Lawrence Berkeley National Laboratory, Berkeley, CA 94720, USA. [4]Stanford Institute for Materials and Energy Science, SLAC National Accelerator Laboratory, 2575 Sand Hill Road, Menlo Park, CA 94025, USA.
*These authors contributed equally to this work.
†Corresponding author. Email: yicui@stanford.edu

Herein, an optical cell was built for real-time imaging and monitoring of the sulfur evolution processes to understand the reaction mechanism (Fig. 1A). By combining in situ optical microscopy study, ex situ morphological and structural characterization, electrochemical property tests, and theoretical calculations, we systematically investigate the sulfur growth behaviors on different current collectors and correlate the results with their electrochemical performance. We visualize both solid sulfur crystals emerging on carbon surfaces and liquid sulfur droplets growing on nickel (Ni) substrates during charging at room temperature. The liquid state of sulfur enables high mobility and fast phase transition, thus accelerating the redox chemistry and improving kinetics during the battery cycling (Fig. 1B). Therefore, the reversible capacity, reaction kinetics, and cycling life of the liquid sulfur are greatly improved compared with that of the solid sulfur. In addition, we demonstrate that the dead Li_2S, which is the primary cause of the increased polarization and decreased capacity upon cycling, can be catalytically decomposed by Ni. Last, we design lightweight, three-dimensional (3D) Ni-coated melamine foam as advanced electrodes for high-rate and long–cycle life Li-S batteries (Fig. 1B).

RESULTS AND DISCUSSION

To evaluate the effect of current collector materials on electrochemical performance, Ni-coated (~50 nm) aluminum (Al) foil was fabricated through electron-beam evaporation (denoted as Ni), commercial carbon-coated Al (denoted as C), and Al foils were used as current collectors for Li-S batteries. Coin cells were assembled with lithium polysulfide catholyte using Li metal as the anode and different planar current collectors at the cathode. Galvanostatic charge/discharge and cyclic voltammetry (CV) measurements were carried out to evaluate the battery performance. The discharge profiles at 0.05 mA cm^{-2} for the Ni current collector consist of two plateaus at 2.3 to 2.4 V and 2.1 V (fig. S1A), which correspond to the reduction of Li_2S_8 to long-chain Li_2S_6/Li_2S_4 and the formation of Li_2S_2/Li_2S, respectively (*33*). In the charging process, the two plateaus represent the conversion from lithium sulfides to polysulfides and lastly to sulfur (*2*). These plateaus are also stable in the following cycles with a relatively low polarization, suggesting a kinetically efficient reaction process. In contrast, the C electrode exhibits large polarization with lower discharge potentials and higher charge potentials as well as increasing overpotentials in the subsequent cycles (fig. S1B). As for the Al current collector, a much lower capacity was observed, indicating the inactivity of the Al surface for polysulfide conversion reaction (fig. S2A). Moreover, the charge/discharge plateaus even disappeared starting from the second cycle, indicating high polarization and slow redox reaction kinetics (fig. S1C). The CV curves of the battery based on Ni, C, and Al current collectors were conducted in the potential window between 1.0 and 3.0 V at a scan rate of 0.1 mV s^{-1} for three cycles, and the corresponding results are shown in fig. S1 (D to F). The Ni substrate exhibits higher peak currents, sharper redox peaks, and smaller polarization compared to C and Al substrates, demonstrating facilitated polysulfide conversion kinetics on the Ni surface that corroborate the galvanostatic charge/discharge results (fig. S1, A to C).

The cycling performance of Li-S batteries based on Ni, C, and Al electrodes are shown in fig. S2B. A capacity of 0.98 mAh cm^{-2} was delivered for the Ni electrode at a current density of 0.05 mA cm^{-2}, which retained 95% of its capacity (0.93 mAh cm^{-2}) after 50 cycles (fig. S2B), demonstrating good cycling stability. However, the capacity decayed quickly from 1.12 to 0.16 mAh cm^{-2} for the C electrode with a capacity retention of only 14% when tested at the same conditions. This capacity decay is mainly ascribed to the weak binding between carbon and lithium polysulfides causing the dissolution of polysulfides (*13*). Meanwhile, almost no redox reactions occurred on the Al surface, which showed a capacity close to zero after three cycles, indicating the nonactive surface of Al foil. When the current density was increased five times to 0.25 mA cm^{-2}, the battery with a Ni electrode still delivered a capacity of 0.77 mAh cm^{-2}, 69% of the capacity obtained at 0.05 mA cm^{-2} (fig. S2C), indicating a fast charge/discharge capability, while C and Al electrodes could not work at this current density. Electrochemical impedance spectroscopy (EIS) was performed to further understand the charge transfer and resistance of these electrodes. Figure S2D and inset show the Nyquist plots of the cells with Ni, C, and Al electrodes at open circuit before cycling. The depressed semicircle represents the charge transfer resistance (R_{ct}) on the electrode surface (*34*). It can be clearly seen that the R_{ct} of the Ni electrode is much lower than that of the C and Al electrodes (fig. S2D). The smaller resistance indicates that the Ni layer exhibits faster charge transfer compared to that of the other electrodes, which will be further confirmed by theoretical calculations of the lithium ion charge transfer kinetics in later discussion.

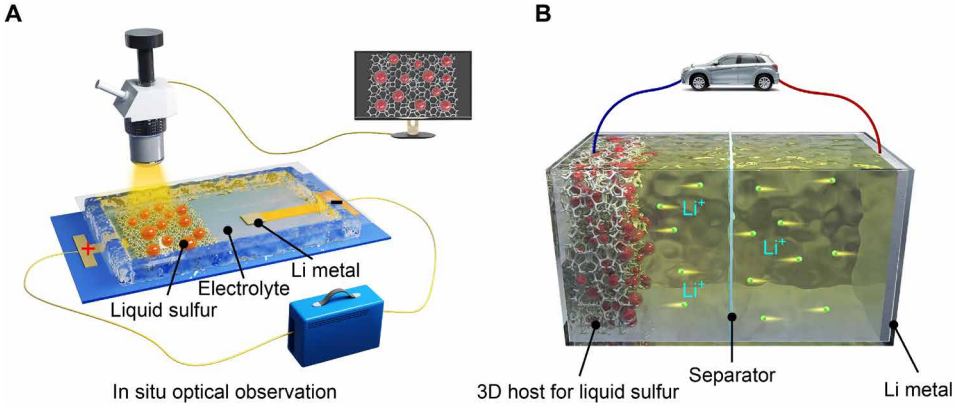

Fig. 1. Supercooled liquid sulfur for Li-S batteries. (**A**) In situ optical observation of sulfur evolution processes. (**B**) Design of three-dimensional (3D) electrodes for high-performance Li-S batteries.

To further understand the notably different battery performance of these electrodes, in situ optical observation and ex situ experimental characterizations are combined to reveal the underlying mechanism. As sulfur species are sensitive to the atmosphere (e.g., water and oxygen), e-beam, and x-ray irradiation (*32*), in situ optical microscopy is a mild and effective methodology to monitor the morphology evolution of sulfur species on different current collectors. As demonstrated in fig. S3 and movies S1 and S2, distinct sulfur growth behaviors were observed on Ni, C, and Al electrodes. As seen from fig. S3 (A to C), there was no sulfur growth or Li_2S deposition on the surface of Al over the entire range of applied voltage (from 1.0 to 3.0 V), suggesting the inertness of Al surface for sulfur redox. In contrast, many sulfur crystals (highlighted by the red circle) emerged and grew on the surface of the C electrode during charging (fig. S3E and movie S1). The subsequent discharge process was also monitored, and a large number of flocculent, blurry particles precipitated out during the process (fig. S3F and movie S1). Spherical liquid sulfur droplets gradually nucleated and grew on the Ni substrate during charging (formation starts at ~2.7 V), and all the sulfur droplets dissolved and lastly disappeared from the Ni surface during the discharging process (fig. S3, G to I, and movie S2). No clear features of Li_2S were visible after discharge, suggesting that the size of the Li_2S is possibly below the resolution limit of the optical microscope. Therefore, scanning electron microscopy (SEM) was used to investigate the morphology change for the sulfur species on different substrates.

The cells based on the Ni, C, and Al electrodes were disassembled in the glovebox at the charged state (3.0 V) or the discharged state (1.0 V), washed using dioxolane, and examined by SEM. The morphologies of the sulfur species are displayed in fig. S4. The Al surface is relatively inert with an ultralow capacity (fig. S1C), and with only a thin layer of sulfur/Li_2S coating the surface during charging and discharging (fig. S4, A and D). This is confirmed by the energy-dispersive x-ray spectrometry (EDS) elemental analysis, which shows a very weak sulfur signal coexisting with peaks from aluminum and oxygen (fig. S5, A and D). In contrast, large amounts of flower-shaped Li_2S particles composed of small sheets with sizes of about 2 to 3 μm were observed under SEM that randomly deposited on the surface of the C electrode during discharging (figs. S4B and S5B). After charging to 3.0 V, in addition to the sulfur crystals produced by oxidation of Li_2S, some of the insoluble, flower-like Li_2S deposits remained on the carbon surface (inset of fig. S4E and fig. S5E). These insoluble Li_2S causes capacity decay due to irreversible sulfur conversion reactions, which is consistent with the cycling results (fig. S2B). High density of vertically grown Li_2S nanosheets was observed for the Ni electrode during the discharging process (figs. S4C and S5C), and the SEM image (fig. S4F) combined with EDS spectrum (fig. S5F) indicates the complete conversion from Li_2S nanosheets to sulfur on the Ni surface after charging to 3.0 V. This reversible deposition/dissolution of the sulfur species on the Ni surface is critical to maintain efficient charge transfer kinetics and achieve a long-term cycling stability for Li-S batteries.

To obtain a more detailed understanding of the Li_2S oxidation process, x-ray photoelectron spectroscopy (XPS) was used to analyze the products on Ni and C substrates at the charged states. In the high-resolution Li 1s spectrum, it is worth noting that no obvious features can be observed in the lithium signal from the Ni sample, indicative of the absence of/little lithium polysulfide intermediates or Li_2S after the charging process (fig. S4G). However, the distinct lithium signal at around 55.3 eV can be clearly seen from the C sample (fig. S4G) (*35*), implying the existence of lithium sulfides that match well with the SEM results (fig. S4E). As for the S 2p spectrum of the charged C electrode shown in fig. S4H, other than the peaks that correspond to elemental S (162.7 and 163.9 eV), the appearance of S^{2-} peaks (160.6 and 161.8 eV) in the XPS spectra, corresponding to Li_2S, indicates the existence of remaining Li_2S covering the surface of the carbon current collector (*36*). As for the Ni current collector, besides the peaks that can be ascribed to S^0 (fig. S4H), which confirm the conversion of polysulfides to sulfur, there is another peak located at 161.6 eV that can be assigned to the Ni—S bond formed at the interface (*37*). Therefore, the Ni layer speeds up not only the electron transfer but also the redox reaction of the polysulfide conversion on the electrode surface, which is expected to promote the reversibility of sulfur chemistry and enable high-power capability for Li-S batteries.

On the basis of the above discussion, Fig. 2 (A to C) presents schematics of the sulfur species evolution on Ni, C, and Al substrates during the charging and discharging processes. During the charging process, some sulfur droplets start to nucleate on the surface of the Ni electrode. These liquid droplets are generated at small sizes, then grow up and merge together into larger sizes after touching each other. The liquid sulfur droplets leave plenty of unoccupied current collector surface as electrochemically active sites for polysulfide conversion, which enables the high area capacity on the Ni surface (fig. S1A). Upon discharging, the liquid sulfur droplets reversibly reduce into soluble polysulfides and lastly form sheet-like Li_2S depositing on the Ni surface (Fig. 2A). In contrast, on the C substrate, the accumulation of insulating Li_2S and disconnected sulfur crystals during repeated cycling will block charge transport across the electrode/electrolyte interface and cause active material loss, resulting in poor reaction kinetics and fast capacity decay (Fig. 2B). For Al substrates, there is generally a thin and dense oxidation layer (Al_2O_3) on the surface, which weakens the adsorption of sulfur species on the interface, rendering the surface inert to sulfur conversion. Therefore, the thin layer of insulating sulfur/Li_2S on the inactive interface passivates the electrode, terminating further accumulation of sulfur species and leading to the negligible capacity in charging/discharging processes (Fig. 2C).

To reveal the mechanism underneath different sulfur growth behaviors on these three substrates, we performed a series of density functional theory (DFT) calculations. On the basis of the calculation results, the adsorption energy of S_8 on a graphene basal plane (E_{ad} = −0.81 eV, fig. S6) is much weaker than that on the edge (E_{ad} = −5.44 eV). Therefore, S_8 will tend to bind on the edge as shown in Fig. 2D. The very strong binding energy of S_8 on graphene edge breaks the S_8 rings into chains, which function as nuclei for sulfur crystals. Meanwhile, the enhanced electric field at the edges also facilitates the generation of S_8 molecules and crystallization of sulfur. As for Ni and Al substrates, a thin oxidation layer was assumed to be on the metal surface before sulfur evolution. Here, Ni (111) and Al (111) covered by one layer of oxygen are constructed to simulate these two metal substrates as shown in Fig. 2 (E and F). Ni (111) and Al (111) configurations are picked for the DFT calculations because (111) face is the most efficient way of packing atoms within a single layer in face-centered cubic (fcc) metals and (111) is the most stable surface in fcc metals as well. In the Al case, the oxygen adheres strongly to the surface of Al, forming a very compact (only 0.72 Å in thickness as shown in fig. S7B) and impermeable

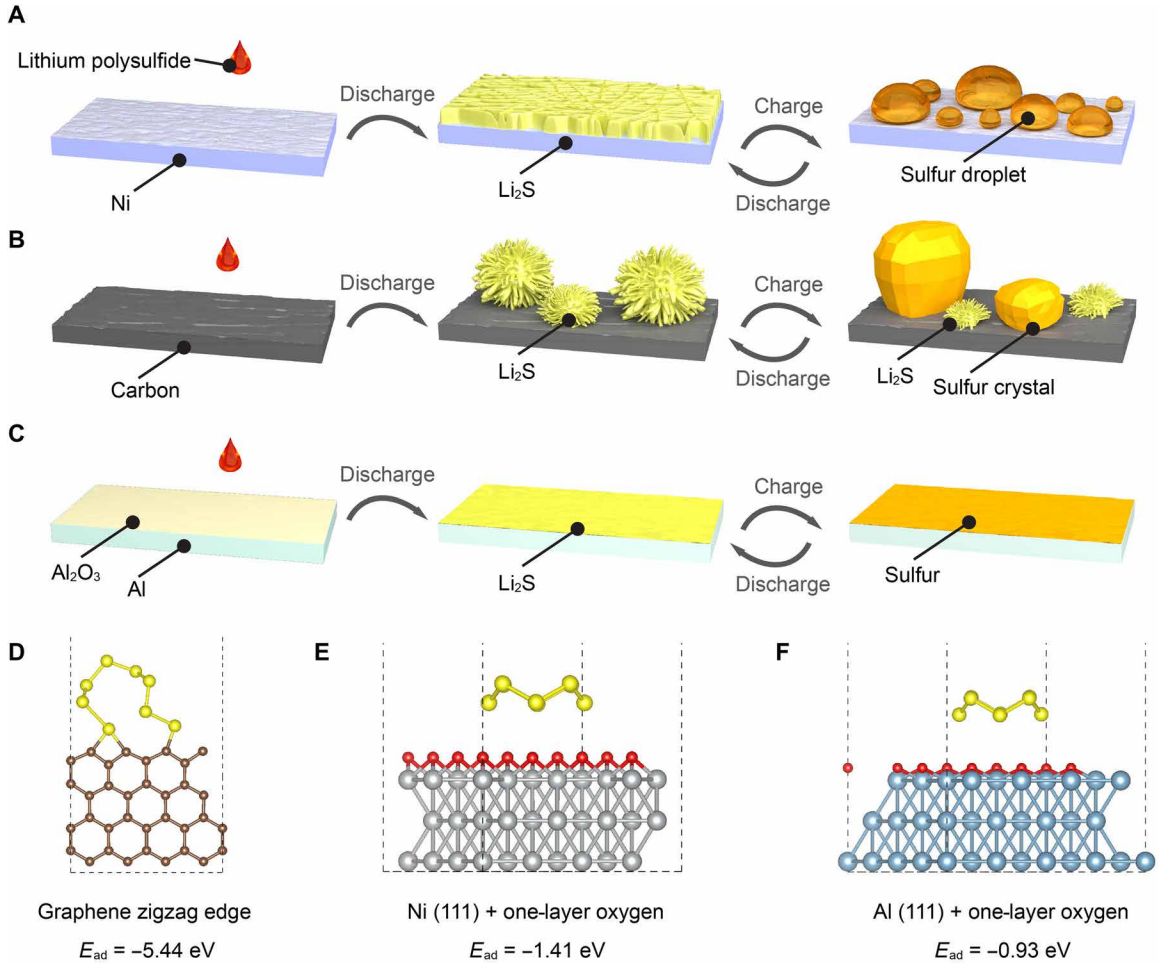

Fig. 2. Schematic of sulfur evolution and mechanism understanding by theoretical calculations. Schematic illustration of the sulfur species evolution on (**A**) Ni, (**B**) C, and (**C**) Al substrates during charging and discharging processes. Adsorption energy and configuration of S_8 adsorbed on (**D**) graphene zigzag edge, (**E**) nickel (111) surface covered by one layer of oxygen, and (**F**) aluminum (111) surface covered by one layer of oxygen.

Al-O layer, which contributes to its inertness to foreign chemical compounds, such as S_8. The weak interaction between S_8 and the Al substrate (E_{ad} = −0.93 eV) is consistent with the phenomenon of no obvious sulfur growth on the Al. On the other hand, the Ni—O bonds are much weaker than the Al—O bonds. Therefore, the Ni-O layer, 1.10 Å in thickness (fig. S7A), is much looser than the Al-O layer, which induces stronger interactions between S_8 and the Ni substrate (E_{ad} = −1.41 eV). This interaction is moderate for sulfur droplet formation and explains the results discussed above.

The distinct Li-S battery performance induced by different current collectors inspires us to consider three questions: (i) Can the battery performance be improved by simple cast coating of sulfur electrodes on the Ni current collectors? (ii) Can the sulfur growth behaviors observed on 2D substrates be extended to 3D structures? (iii) Is the different battery performance related to the states of liquid or solid sulfur? To answer the first question, Ni, C, and Al were used as the cathode current collectors with sulfur [70 weight % (wt %) sulfur, 20 wt % carbon black, and 10 wt % polyvinylidene fluoride (PVDF)] coated on them as the active materials. The cycling stability of the Li-S battery with these three substrates was tested at a rate of 0.2C for 100 cycles. The battery with sulfur coated on the Ni substrate exhibits obviously improved capacity and Coulombic efficiency (retained capacity of 580 mAh g^{-1} with Coulombic efficiency above 99%) upon cycling compared to the conventional C-based (427 mAh g^{-1} with Coulombic efficiency above 96%) and Al-based (367 mAh g^{-1} with Coulombic efficiency above 95%) electrodes (fig. S8). These results further confirm that the Ni coating layer facilitates fast transport of electrons and lithium ions and promotes the redox of sulfur species, which is responsible for the enhanced capacity and stability of the electrode.

To understand the second question, we chose Ni foam and carbon-coated Ni foam as the 3D porous architecture to reveal the sulfur growth behavior and distinguish the battery performance. Ni foam can be used as a template for the growth of graphene on its surface by chemical vapor deposition (CVD) (*38*), thus enabling the comparison between 3D Ni foam and graphene-coated nickel (G/Ni) foam. Compared to the pristine Ni foam, wrinkled graphene layers adhered to the surface of Ni foam can be clearly observed after CVD growth (Fig. 3, A and E). Raman spectroscopy is a powerful tool to identify the detailed structure and quality of graphene. Figure S9 exhibits the Raman spectra of the Ni foam and G/Ni

foam. There is no Raman signal for the metallic Ni, while three Raman features appear referring to the D band at ~1350 cm^{-1}, G band at ~1580 cm^{-1}, and the 2D band at ~2710 cm^{-1} (*39*, *40*). The low intensity of the defect-related D band and symmetrical 2D and G bands indicate the high quality of the graphene grown on the Ni foam. To obtain a more complete understanding of the reaction mechanism and to analyze the morphology change of sulfur on the 3D Ni foam and G/Ni framework, the transparent cell was used to monitor the sulfur evolution in real time under battery operation. Figure 3 (B to D) presents optical images of a Ni foam electrode at initial, charged, and discharged states. Initially, the Ni foam was immersed in the polysulfides (Fig. 3B), and sulfur droplets were observed and grew large during the charging process. Two droplets touching with each other merged together and became a larger one (Fig. 3C and movie S3). We have recently performed in situ x-ray absorption spectroscopy measurements and confirmed that the liquid droplets are sulfur in composition (*41*). It cannot be ruled out that trace amounts of electrolyte impurities maybe solvated in the liquid sulfur droplets; however, their concentration should be low on the basis of our previous results including Raman spectroscopy, rapid solidification of liquid droplet, and melting point measurement (*32*). The sulfur droplets were gradually dissolved into the electrolyte and completely disappeared at the end of the discharge process (Fig. 3D and movie S4). The sulfur dissolution and reformation can be well controlled and repeated during tens of charge/discharge cycles. In contrast, the irregular sulfur crystals slowly grow and randomly distributed on the surface of G/Ni foam as displayed in Fig. 3 (F and G). The sulfur crystals slowly dissolve into the electrolytes during discharge and lastly disappeared upon discharging to 1.5 V (Fig. 3H and movies S5 and S6). The liquid sulfur droplets grow faster than sulfur crystals at the constant voltage charging process, in which at the same charging time the Ni foam electrode produces more nuclei and faster growth of sulfur (Fig. 3, I to L, and movie S7) than that of G/Ni foam (Fig. 3, M to P, and movie S8), indicating the faster kinetics of liquid sulfur that is beneficial for fast charging.

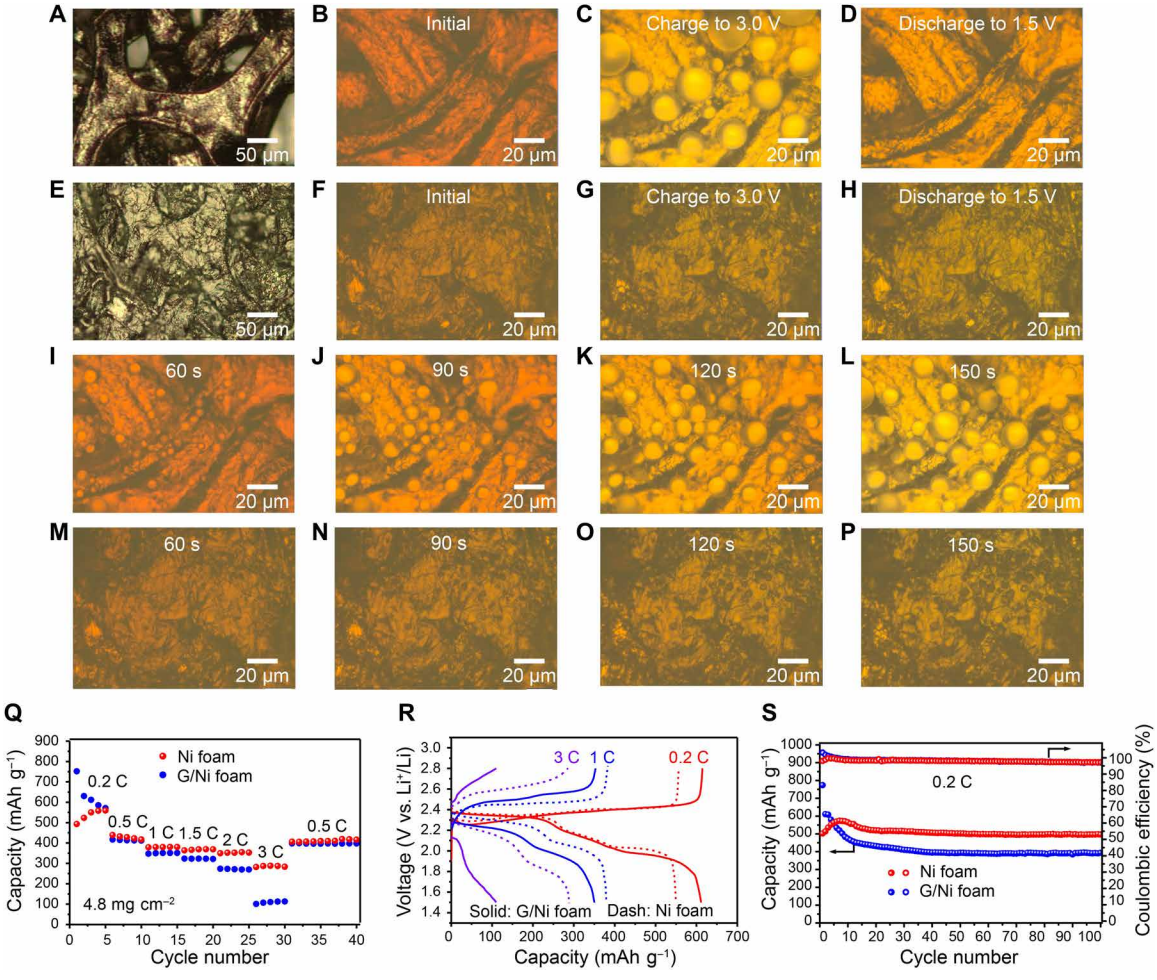

Fig. 3. In situ optical observation and electrochemical performance of the Ni foam and G/Ni foam electrodes in lithium polysulfide electrolyte. Optical images of (**A**) Ni foam. Optical images of Ni foam in lithium polysulfide electrolyte (**B**) at initial state, (**C**) after charging to 3.0 V, and (**D**) discharging to 1.5 V. (**E**) G/Ni foam. Optical images of G/Ni foam in lithium polysulfide electrolyte (**F**) at initial state, (**G**) after charging to 3.0 V, and (**H**) discharging to 1.5 V. Snapshots of the constant voltage charging process for Ni foam electrode at (**I**) 60 s, (**J**) 90 s, (**K**) 120 s, and (**L**) 150 s. Snapshots of the constant voltage charging process for G/Ni foam electrode at (**M**) 60 s, (**N**) 90 s, (**O**) 120 s, and (**P**) 150 s. (**Q**) Rate performance of the Ni foam and G/Ni foam electrodes at different current densities. (**R**) Charge/discharge voltage profiles of the Ni foam (dash line) and G/Ni foam (solid line) electrodes at 0.2, 1, and 3 C. (**S**) Cycling performance and Coulombic efficiency of the Ni foam and G/Ni foam electrodes at 0.2 C for 100 cycles.

The electrochemical properties of Ni and G/Ni foams were measured in coin cells to verify whether the liquid or solid state of sulfur affects the battery performance, as posed in the third question. Figure 3Q shows the rate performance of the cells at various current rates (from 0.2 to 3 C, 1 C = 1675 mA g^{-1}) between 1.5 and 2.8 V. The 3D Ni foam electrode demonstrates good rate performance with capacities of around 360 and 300 mAh g^{-1} at 2 C and 3 C, respectively, whereas the cell with the G/Ni foam electrode only maintains capacities of 275 and 110 mAh g^{-1} (fig. S10, A and B). The corresponding charge-discharge profiles at 0.2 C, 1 C, and 3 C for Ni and G/Ni foam electrodes are compared in Fig. 3R. It can be seen that the voltage hysteresis between charge/discharge is much smaller for Ni foam compared to that of the G/Ni foam electrode, which shows large polarization. The CV curves of the Ni foam electrode have sharper and narrower peaks than those of the G/Ni foam, confirming its improved kinetics (fig. S10, C and D). Moreover, the cell with the Ni foam electrode retains two distinct discharge voltage plateaus even at 3C, while there is almost no discharge plateau for the G/Ni foam electrode at the same current density (Fig. 3R). Meanwhile, Ni foam also shows outstanding cycling stability and retains a capacity of 500 mAh g^{-1} over 100 cycles with a Coulombic efficiency of approximately 99% (Fig. 3S). The slight capacity increase in the first few cycles is possibly due to gradual wetting of some previously inaccessible areas in the Ni foam electrode. This phenomenon was also reported in previous papers on thick or high sulfur–loading electrodes that require some time for sulfur/polysulfide activation (*42*, *43*). Conversely, the battery with the G/Ni foam electrode exhibits rapid capacity decay upon cycling with a capacity retention of only 50%, which is due to the weak polysulfide adsorption on the carbon surface leading to inevitable polysulfide dissolution into the electrolyte. The impressively improved cycle performance and rate capability of the Ni foam–based electrode as compared to that of the G/Ni electrodes arise from the chemisorption of polysulfides by the Ni framework and the accelerated kinetics between liquid sulfur and liquid polysulfides on the surface of the Ni electrode.

To gain a deeper insight and understand the mechanism of why Ni-based electrodes show better battery performance as compared with carbon electrodes, we studied the decomposition of Li_2S on the Ni surface, graphene basal plane, and graphene edge through DFT calculations. The overall Li_2S decomposition includes two elemental steps: One Li atom dissociates from Li_2S and the dissociated Li diffuses away from the LiS cluster. The barriers of these two elemental steps are obtained via the climbing-image nudged elastic band (CI-NEB) method as shown in Fig. 4A. It is well known that the reaction barriers are very sensitive to the adsorption energy of key intermediates (*44*). The adsorption energy of Li_2S (the key intermediate) on substrates is considered as an important parameter to explain and distinguish Li_2S decomposition behavior on Ni surface, graphene basal plane, and graphene edge. The very strong interaction between Li_2S and the graphene edge (E_{ad} = −6.04 eV, fig. S11) promotes the Li_2S dissociation into Li and LiS but hampers the lithium ion diffusion away from the edge with a barrier of 1.55 eV (Fig. 4B). On the other hand, the interaction of Li_2S with the graphene basal plane (E_{ad} = −0.78 eV, fig. S11) is too weak to activate the Li_2S dissociation. In addition, the dissociation intermediates (Li and LiS) are more unstable on graphene basal plane than that of Li_2S by 1.85 eV (Fig. 4C), indicating that the Li and LiS will be recombined into Li_2S automatically on graphene basal plane. Therefore, the ideal interaction between Li_2S and the substrate material for Li_2S decomposition should be between the range of −0.78 and − 6.04 eV. The interaction of Li_2S on the Ni surface is relatively moderate (E_{ad} = −5.13 eV, fig. S11), and the rate-determining step of Li_2S decomposition exhibits a barrier of 1.07 eV (Fig. 4D). The theoretical calculations combined with the above experimental analysis explain the improved reversibility, active material utilization, and improved electrochemical reaction kinetics on the surface of Ni-based electrodes.

From the above discussion, it is evident that Ni foam can produce liquid sulfur droplets with fast charge/discharge kinetics, but performance is still limited by the surface area with unsatisfactory capacity. It is well known that capacity depends on the accessible surface area of the electrodes. Therefore, it is anticipated that increasing the accessible active sites of the Ni electrode could help increase the polysulfide adsorption and conversion to achieve higher specific capacity. Moreover, using a lightweight current collector is another important parameter for realizing high–specific energy Li-S batteries. With these considerations in mind, to further increase the exposed area of Ni and elucidate effects of increased surface area on improving battery performance, we designed a 3D interconnected Ni network structure by coating Ni on lightweight 3D melamine foam through electroless Ni deposition (Fig. 5, A and B). The optical and SEM images of the nickel-coated melamine foam show that the porous melamine framework was uniformly covered by the Ni materials (Fig. 5, A to C). The nickel-coated melamine foam is much lighter (6 to 7 mg cm^{-2}) compared to the Ni foam (~40 mg cm^{-2}), which exhibits large pores ranging from 100 to 200 μm with a porosity larger than 99%. The interpenetrated porous structure provides abundant space as an electrolyte reservoir, while the downy Ni coating layer enlarges the accessible reaction areas and provides generous amounts of active sites to absorb and facilitate the conversion of sulfur species during cycling. An optical cell was also assembled using a Ni-coated 3D melamine foam electrode, and in situ observation under the optical microscope was conducted to verify that a similar sulfur evolution process as on planar Ni foil and 3D Ni foam occurred (movie S9). As expected, the snapshots of the charging/discharging process shown in Fig. 5D confirm the sulfur droplet formation during charging and dissolution during discharging process. Coin cells were assembled to test the electrochemical properties of the as-prepared Ni-coated melamine foam electrode. The voltage profiles of the cell using lithium polysulfide catholyte at 0.2C for the first 20 cycles are shown in Fig. 5E, which demonstrate well-defined discharge/charge plateaus and good capacity reversibility. The unique lightweight 3D electrode structure enables a high capacity of 1000 mAh g^{-1} at 0.2C, and a reversible capacity of about 450 mAh g^{-1} at a high current density of 2C (Fig. 5F). After adjusting the charging current density back to 0.5C, the capacity was similar to that of the initial cycles, demonstrating good rate capability. In addition, the electrode exhibits good long-term cycling stability with an initial specific capacity of 825 mAh g^{-1}, which stabilizes at ~652 mAh g^{-1} after 200 cycles tested at 0.5C (Fig. 5G). The capacity decay is possibly because the liquid sulfur droplets formed on the Ni surface tend to merge together as they grow large during the charging process; they may get detached from the Ni surface and partly dissolve into the electrolyte when the droplets are too large. Therefore, strategies to control the size of the sulfur droplets and new electrode design to confine sulfur droplets need to be developed. Increasing the surface area of Ni can help increase the nucleation sites of the sulfur droplets and then alter the

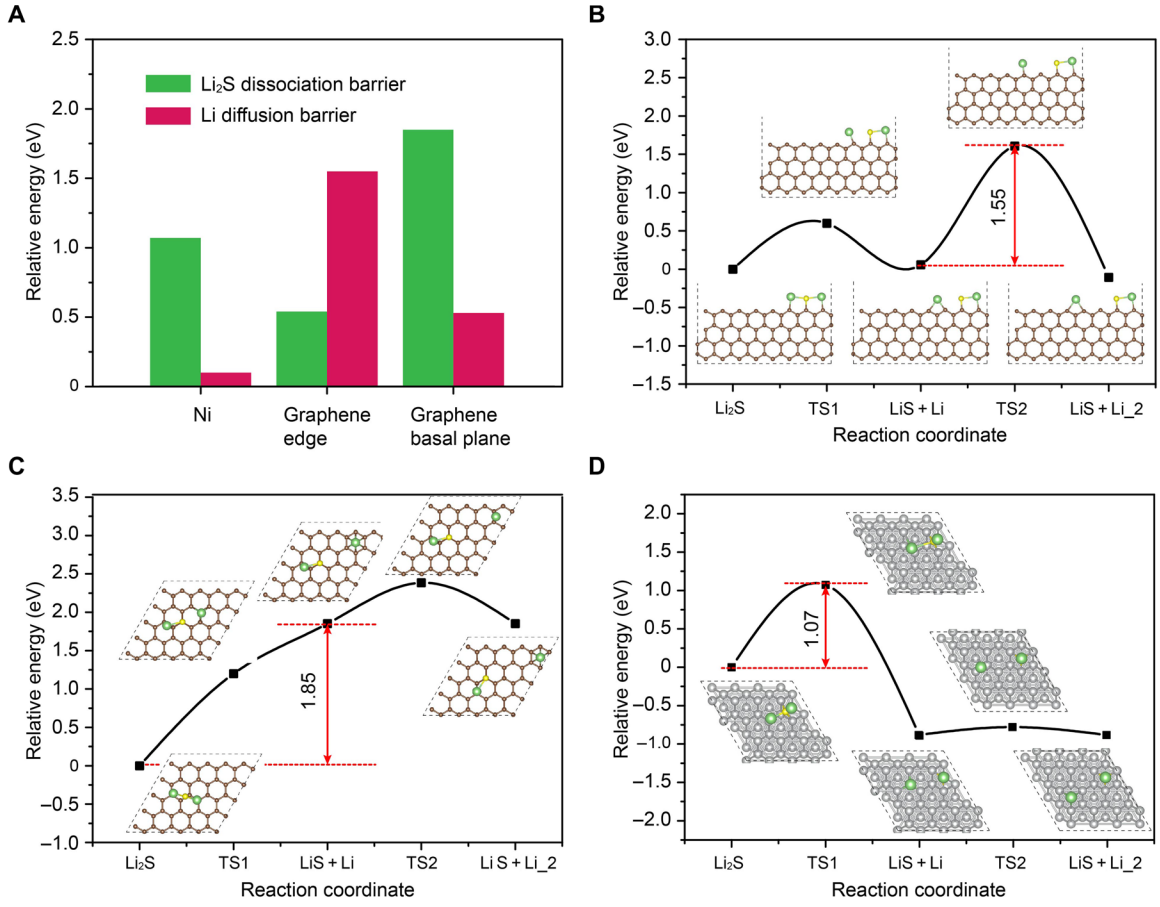

Fig. 4. Li_2S decomposition and lithium ion diffusion barriers on the surface of nickel and graphene. (**A**) Comparison of the Li_2S decomposition and lithium ion diffusion barriers on the surface of nickel, graphene basal plane, and graphene edge. Energy profiles for the decomposition of Li_2S cluster and lithium ion diffusion on the surface of (**B**) graphene edge, (**C**) graphene basal plane, and (**D**) nickel. Inset figures are top-view schematic representations of the corresponding decomposition and lithium ion diffusion pathways for graphene edge, graphene basal plane, and nickel. Here, green, yellow, gray, and beige balls symbolize lithium, sulfur, nickel, and carbon atoms, respectively.

droplet merging behaviors. To further improve the energy density of the electrodes, two layers of Ni-coated melamine foam were stacked to increase the active material loading to 8.0 mg cm^{-2}. This electrode design demonstrates well-retained plateaus from 0.2- to 1 C rate, as shown in fig. S12A, indicating the good reaction kinetics. A high capacity of ca. 900 mAh g^{-1} at 0.2 C and a capacity of 353 mAh g^{-1} was achieved at a high current density of 2 C (fig. S12B). Moreover, the electrode exhibits an initial discharge capacity of 707 mAh g^{-1} at 0.5 C, which stabilizes to around 586 mAh g^{-1} after 100 cycles, corresponding to a capacity decay of 0.17% per cycle (fig. S12C), indicating its good cycling stability. The Ni-coated melamine foam can provide more active sites for sulfur and Li_2S deposition, and the 3D interconnected network is beneficial for electron and ion transport. The interaction between Ni particles and polysulfides can effectively adsorb and convert the polysulfides, which reduces the material loss and improves the utilization of the active materials, resulting in high capacity, high rate, and long cycle life for Li-S batteries. Further design of 3D interconnected, hollow confined architecture with inner surface coated with Ni that facilitates the growth of sulfur droplets, while the outer surface covered with Al that inhibits the growth of sulfur, can confine the sulfur droplets inside the hollow structure to further extend the cycle life of Li-S batteries.

CONCLUSIONS

In summary, in situ optical microscopy combined with ex situ analyses and DFT theoretical calculations were used to systematically investigate and correlate the sulfur evolution on different current collectors with their electrochemical performance. Different sulfur growth behaviors were visualized in real time during battery operation: Solid sulfur crystals were produced on the carbon surface and supercooled liquid sulfur droplets formed on the Ni surface at room temperature. The batteries with liquid sulfur droplets deliver better reversible capacity, faster reaction kinetics, and longer cycling life as compared to solid sulfur. We explained the distinct battery performance from the aspects of sulfur adsorption binding energy, polysulfide conversion, Li_2S decomposition, and lithium ion diffusion energy barriers. The strong coupling between Ni and lithium polysulfides helps suppress polysulfide dissolution, improves the utilization of sulfur, and accelerates the kinetics of phase conversion, which are essential aspects of realizing stable and fast-charging Li-S batteries. On the basis of these fundamental understandings, 3D Ni-based interconnected architectures are designed to provide a large active surface area for sulfur/Li_2S deposition, fast transport pathways for both electrons and Li ions, and a route for Li_2S/sulfur transformation toward the development of high-energy and long-life Li-S batteries.

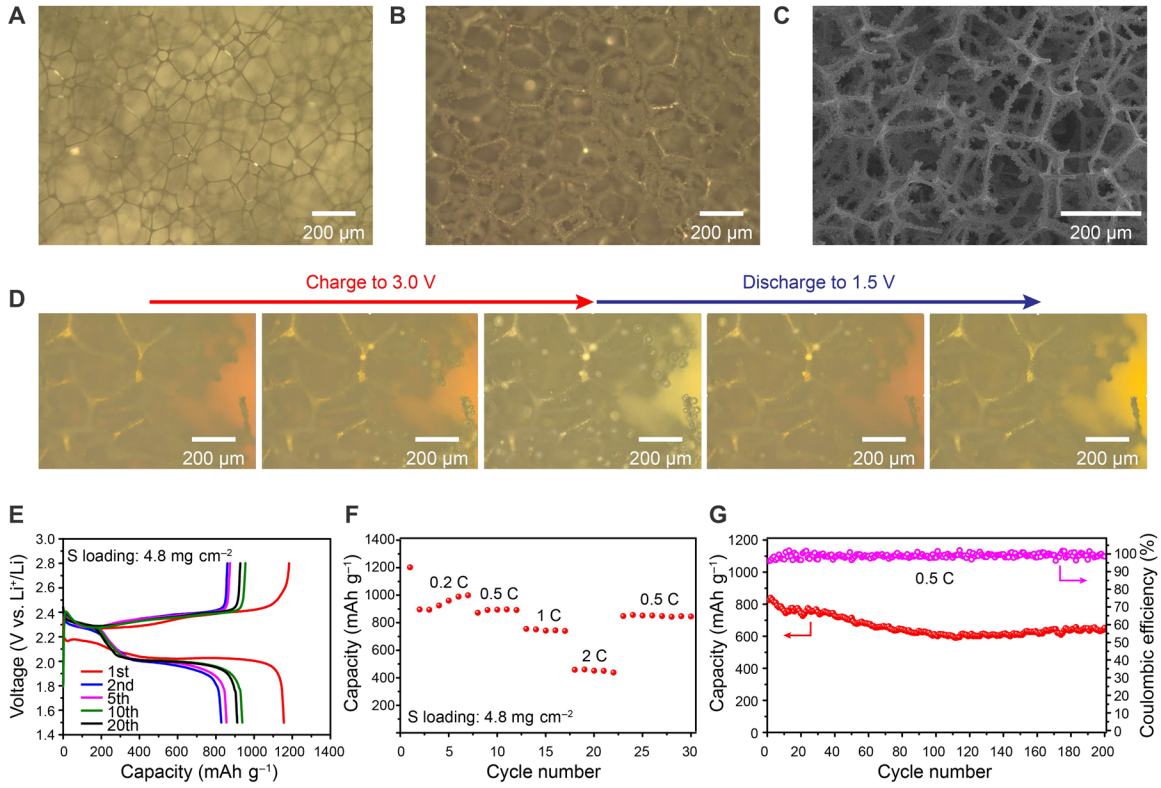

Fig. 5. Morphology and electrochemical performance of lightweight nickel-coated melamine foam. Optical images of (**A**) melamine foam and (**B**) nickel-coated melamine foam. (**C**) SEM image of the nickel-coated melamine foam. (**D**) Optical images of nickel-coated melamine foam in lithium polysulfide electrolyte during charging and discharging. (**E**) Charge/discharge voltage profiles of the nickel-coated melamine foam electrode at 0.2C within a potential window of 1.5 to ~2.8 V versus Li^+/Li^0. (**F**) Rate performance of the nickel-coated melamine foam electrode at different current densities. (**G**) Cycling performance and Coulombic efficiency of the nickel-coated melamine foam electrode at 0.5C for 200 cycles.

MATERIALS AND METHODS

Preparation of Ni electrode

Ni metal was deposited on top of Al foil by an e-beam evaporator with vacuum pressure under 1×10^{-6} torr and at a rate of 0.3 Å s^{-1}.

Preparation of 3D Ni-coated melamine electrode

In a typical synthesis, five pieces of melamine sponge were dispersed in 100 ml of deionized (DI) water. One milliliter of tris-buffer [1.0 M (pH 8.5), Teknova] and 0.2 g of dopamine hydrochloride (Sigma-Aldrich) were sequentially added to the aqueous solution and stirred at room temperature for 1 hour. This formed a very thin layer of polydopamine that helped the Ni nucleation. The samples were then collected and washed three times with DI water. Electroless Ni solution was prepared by dissolving nickel sulfate hexahydrate (20 g $liter^{-1}$), sodium citrate dihydrate (10 g $liter^{-1}$), and lactic acid in DI water (5 g $liter^{-1}$). The polydopamine-coated melamine sponges were immersed in 180 ml of the electroless Ni solutions. Then, 1 g of dimethylamine borane (Sigma-Aldrich) and 2 ml of ammonium hydroxide ($NH_3 \cdot H_2O$, Sigma-Aldrich, 28%) were added to the electroless Ni solution and stirred at room temperature for 10 min. The resulting sponges were washed twice with ethanol and dried in a vacuum oven at 60°C for 1 hour.

Materials characterization

The morphology and microstructure of the samples were investigated by an FEI XL30 Sirion scanning electron microscope operated at an accelerating voltage of 5 kV. Raman spectroscopy was performed on a HORIBA Scientific LabRAM HR Evolution spectrometer with 532-nm excitation. XPS analysis was performed with an SSI SProbe XPS spectrometer with monochromatic Al Kα (1486.6 eV) radiation.

Preparation of the blank electrolyte and polysulfide electrolyte

The blank electrolyte was prepared by dissolving an appropriate amount of lithium trifluoromethanesulfonate (LiTFSI, 1 M) in the solution of 1:1 v/v dimethyl ether (DME) and 1,3-dioxolane (DOL) containing 2 wt % $LiNO_3$. $LiNO_3$ was added to passivate the Li metal surface and suppress its reaction with polysulfides. The polysulfide electrolyte is prepared by chemically reacting Li_2S and sublimed sulfur in the blank electrolyte at a temperature of 60 °C to form Li_2S_8 (5 M). The solution is stirred in an argon-filled glove box to form a brownish-red Li_2S_8 electrolyte solution.

Electrochemical measurements

Electrochemical experiments were performed using CR2032 coin cells assembled in an argon-filled glovebox with lithium metal as the counter and reference electrodes. The Ni foam and G/Ni foam electrodes were cut and pressed before assembling lithium polysulfide cells. Blank electrolyte (20 μl) is added to wet the lithium electrode. Then, a Celgard 2400 separator was placed on top of the lithium electrode. Li_2S_8 electrolyte (30 μl; 5 M, equal to 4.8 mg cm^{-2} sulfur) is

added on the Ni foam or G/Ni electrodes, which is placed in the middle of polytetrafluoroethylene O-ring. Then, the coin cell is lastly compressed with a hydraulic coin cell crimping machine. The sulfur electrodes were prepared by mixing sulfur powder (70 wt %), carbon black (20 wt %), and PVDF binders (10 wt %) in *N*-methyl-2-pyrrolidinone solvent to form a homogeneous slurry and coating onto Al, C, and Ni current collectors. The electrode was dried at 60 °C under vacuum for 12 hours, and the sulfur mass loading of the electrodes ranged from 2.0 to 2.5 mg cm^{-2}. The corresponding specific capacities were calculated on the basis of the weight of sulfur in the cathodes. The electrolyte (20 μl) was added to wet the sulfur cathode. The Celgard 2400 separator was then placed over the electrode, and an additional 20 μl of the blank electrolyte was added to the cell. The lithium-metal foil anode was placed on top of the separator. Galvanostatic charge-discharge cycles were performed on a CT2001A cell test instrument (Land Electronic Co.) The sulfur cathode–based cells were measured with the potential range of 1.5 to 2.8 V (versus Li^+/Li^0). The C-rate for tests was referred to the mass of sulfur in the cathode and was varied from 0.2 to 3 C rate (1 C = 1675 mA g^{-1}). EIS data were obtained with a VMP3 potentiostat (BioLogic) from 200 KHz to 100 mHz with an AC voltage amplitude of 10 mV at the open-circuit potential. CV measurements were performed on a VMP3 potentiostat (BioLogic) from 1.0 to 3.0 V with a scan rate of 0.1 mV s^{-1}. For the cycled samples, the cells were disassembled inside an Ar-filled glove box, and the electrodes were washed with dioxolane to remove the lithium salt and dried inside the glove box at room temperature before analysis.

Optical cell fabrication

The cell was assembled inside an Ar-filled glovebox. Al, C, and Ni electrodes were used as the working electrodes. For 3D electrodes, Ni foam, G/Ni foam, and Ni-coated melamine foam were used as the working electrodes. Li metal was laminated onto the copper foil and used as the counter electrode. A cover glass slide was placed on top of the electrodes, and the cell was then sealed by a thermoplastic ionomer (Meltonix 1170-60, Solaronix), leaving two small openings for filling liquid electrolyte. Li_2S_8 (0.5 or 2.5 M) dissolved in DOL/DME (1:1 v/v) with 1 M LiTFSI and 2 wt % $LiNO_3$ additive was used as the catholyte. After filling the electrolyte, epoxy was used to lastly seal the remaining two openings.

In situ optical observation of sulfur growth

In situ electrochemical reaction was performed with an MTI eight-channel battery tester, while being imaged at the same time using light microscope equipped with air-immersion objective (LMPLFLN-BD, Olympus, 50×, numerical aperture of 0.5, working distance of 10.6 mm), broadband Xenon lamp, and CMOS detector. The image series were taken with a frame rate of one frame per second, and the spatial resolution of the microscope is ~500 nm. Galvanostatic charging/discharging was used to produce and dissolve the sulfur.

Theoretical calculations

The DFT calculations were carried out by using the Vienna Ab initio Simulation Package (*45*, *46*). The exchange-correlation interaction is described by generalized gradient approximation with the Perdew-Burke-Ernzerhof functional (*47*). The van der Waals interaction was described by using the empirical correction in Grimme's scheme, i.e., DFT + D_3 (*48*). The energy cutoff was set to 500 eV. In addition, a vacuum region of 15 Å was used to avoid the interactions among the periodic slabs. The CI-NEB method was used to find saddle points and minimum energy paths (*49*). In all our calculations, atoms in the fixed region are held fixed at the bulk positions, while the atoms in the buffer and vacuum regions are fully relaxed until all force components acting on the atoms are below 0.005 eV/Å.

SUPPLEMENTARY MATERIALS

Supplementary material for this article is available at http://advances.sciencemag.org/cgi/content/full/6/21/eaay5098/DC1

REFERENCES AND NOTES

1. P. G. Bruce, S. A. Freunberger, L. J. Hardwick, J.-M. Tarascon, Li–O_2 and Li–S batteries with high energy storage. *Nat. Mater.* **11**, 19–29 (2012).
2. A. Manthiram, Y. Fu, S.-H. Chung, C. Zu, Y.-S. Su, Rechargeable Lithium–Sulfur batteries. *Chem. Rev.* **114**, 11751–11787 (2014).
3. Y. Liu, G. Zhou, K. Liu, Y. Cui, Design of complex nanomaterials for energy storage: Past success and future opportunity. *Acc. Chem. Res.* **50**, 2895–2905 (2017).
4. W. J. Chung, J. J. Griebel, E. T. Kim, H. Yoon, A. G. Simmonds, H. J. Ji, P. T. Dirlam, R. S. Glass, J. J. Wie, N. A. Nguyen, B. W. Guralnick, J. Park, Á. Somogyi, P. Theato, M. E. Mackay, Y.-E. Sung, K. Char, J. Pyun, The use of elemental sulfur as an alternative feedstock for polymeric materials. *Nat. Chem.* **5**, 518–524 (2013).
5. Y. Yang, G. Zheng, S. Misra, J. Nelson, M. F. Toney, Y. Cui, High-capacity micrometer-sized Li_2S particles as cathode materials for advanced rechargeable Lithium-Ion batteries. *J. Am. Chem. Soc.* **134**, 15387–15394 (2012).
6. Q. Pang, X. Liang, C. Y. Kwok, L. F. Nazar, Advances in lithium–sulfur batteries based on multifunctional cathodes and electrolytes. *Nat. Energy* **1**, 16132 (2016).
7. X. L. Ji, K. T. Lee, L. F. Nazar, A highly ordered nanostructured carbon–sulphur cathode for lithium–sulphur batteries. *Nat. Mater.* **8**, 500–506 (2009).
8. N. Jayaprakash, J. Shen, S. S. Moganty, A. Corona, L. A. Archer, Porous hollow carbon@ sulfur composites for high-power lithium–sulfur batteries. *Angew. Chem. Int. Ed.* **50**, 5904–5908 (2011).
9. L. Li, Z. P. Wu, H. Sun, D. Chen, J. Gao, S. Suresh, P. Chow, C. V. Singh, N. Koratkar, A foldable lithium–sulfur battery. *ACS Nano* **9**, 11342–11350 (2015).
10. S. Xin, L. Gu, N.-H. Zhao, Y.-X. Yin, L.-J. Zhou, Y.-G. Guo, L.-J. Wan, Smaller sulfur molecules promise better lithium–sulfur batteries. *J. Am. Chem. Soc.* **134**, 18510–18513 (2012).
11. Y.-S. Su, A. Manthiram, Lithium–sulphur batteries with a microporous carbon paper as a bifunctional interlayer. *Nat. Commun.* **3**, 1166 (2012).
12. J.-Q. Huang, Q. Zhang, F. Wei, Multi-functional separator/interlayer system for high-stable lithium-sulfur batteries: Progress and prospects. *Energy Storage Mater.* **1**, 127–145 (2015).
13. G. Zheng, Q. Zhang, J. J. Cha, Y. Yang, W. Li, Z. W. Seh, Y. Cui, Amphiphilic surface modification of hollow carbon nanofibers for improved cycle life of lithium sulfur batteries. *Nano Lett.* **13**, 1265–1270 (2013).
14. X. Tao, J. Wang, C. Liu, H. Wang, H. Yao, G. Zheng, Z. W. Seh, Q. Cai, W. Li, G. Zhou, C. Zu, Y. Cui, Balancing surface adsorption and diffusion of lithium–polysulfides on nonconductive oxides for lithium–sulfur battery design. *Nat. Commun.* **7**, 11203 (2016).
15. T. Zhou, W. Lv, J. Li, G. Zhou, Y. Zhao, S. Fan, B. Liu, B. Li, F. Kang, Q.-H. Yang, Twinborn TiO_2–TiN heterostructures enabling smooth trapping–diffusion–conversion of polysulfides towards ultralong life lithium–sulfur batteries. *Energ. Environ. Sci.* **10**, 1694–1703 (2017).
16. Z. W. Seh, J. H. Yu, W. Li, P.-C. Hsu, H. Wang, Y. Sun, H. Yao, Q. Zhang, Y. Cui, Two-dimensional layered transition metal disulphides for effective encapsulation of high-capacity lithium sulphide cathodes. *Nat. Commun.* **5**, 5017 (2014).
17. H.-J. Peng, T.-Z. Hou, Q. Zhang, J.-Q. Huang, X.-B. Cheng, M.-Q. Guo, Z. Yuan, L.-Y. He, F. Wei, Strongly coupled interfaces between a heterogeneous carbon host and a sulfur-containing guest for highly stable lithium–sulfur batteries: Mechanistic insight into capacity degradation. *Adv. Mater. Interfaces* **1**, 1400227 (2014).
18. Z. Wang, Y. Dong, H. Li, Z. Zhao, H. Bin Wu, C. Hao, S. Liu, J. Qiu, X. W. Lou, Enhancing lithium–sulphur battery performance by strongly binding the discharge products on amino-functionalized reduced graphene oxide. *Nat. Commun.* **5**, 5002 (2014).
19. W. Li, Q. Zhang, G. Zheng, Z. W. Seh, H. Yao, Y. Cui, Understanding the role of different conductive polymers in improving the nanostructured sulfur cathode performance. *Nano Lett.* **13**, 5534–5540 (2013).
20. G. Zhou, K. Liu, Y. Fan, M. Yuan, B. Liu, W. Liu, F. Shi, Y. Liu, W. Chen, J. Lopez, D. Zhuo, J. Zhao, Y. Tsao, X. Huang, Q. Zhang, Y. Cui, An aqueous inorganic polymer binder for high performance lithium–sulfur batteries with flame-retardant properties. *ACS Cent. Sci.* **4**, 260–267 (2018).

21. Z. Yuan, H.-J. Peng, T.-Z. Hou, J.-Q. Huang, C.-M. Chen, D.-W. Wang, X.-B. Cheng, F. Wei, Q. Zhang, Powering lithium–sulfur battery performance by propelling polysulfide redox at sulfiphilic hosts. *Nano Lett.* **16**, 519–527 (2016).
22. G. Zhou, H. Tian, Y. Jin, X. Tao, B. Liu, R. Zhang, Z. W. Seh, D. Zhuo, Y. Liu, J. Sun, J. Zhao, C. Zu, D. S. Wu, Q. Zhang, Y. Cui, Catalytic oxidation of Li_2S on the surface of metal sulfides for Li–S batteries. *Proc. Natl. Acad. Sci. U.S.A.* **114**, 840–845 (2017).
23. G. Babu, K. Ababtain, K. Y. S. Ng, L. M. R. Arava, Electrocatalysis of Lithium Polysulfides: Current Collectors as Electrodes in Li/S Battery Configuration. *Sci. Rep.* **5**, 8763 (2015).
24. H. Al Salem, G. Babu, C. V. Rao, L. M. R. Arava, Electrocatalytic polysulfide traps for controlling redox shuttle process of Li–S batteries. *J. Am. Chem. Soc.* **137**, 11542–11545 (2015).
25. D. Liu, C. Zhang, G. Zhou, W. Lv, G. Ling, L. Zhi, Q.-H. Yang, Catalytic effects in lithium–sulfur batteries: Promoted sulfur transformation and reduced shuttle effect. *Adv. Sci.* **5**, 1700270 (2018).
26. H. Yuan, X. Chen, G. Zhou, W. Zhang, J. Luo, H. Huang, Y. Gan, C. Liang, Y. Xia, J. Zhang, J. Wang, X. Tao, Efficient activation of Li_2S by transition metal phosphides nanoparticles for highly stable lithium–sulfur batteries. *ACS Energy Lett.* **2**, 1711–1719 (2017).
27. H.-J. Peng, W.-T. Xu, L. Zhu, D.-W. Wang, J.-Q. Huang, X.-B. Cheng, Z. Yuan, F. Wei, Q. Zhang, 3D carbonaceous current collectors: The origin of enhanced cycling stability for high-sulfur-loading lithium–sulfur batteries. *Adv. Funct. Mater.* **26**, 6351–6358 (2016).
28. L. Kong, H.-J. Peng, J.-Q. Huang, Q. Zhang, Review of nanostructured current collectors in lithium–sulfur batteries. *Nano Res.* **10**, 4027–4054 (2017).
29. M. Li, Y. Zhang, Z. Bai, W. W. Liu, T. Liu, J. Gim, G. Jiang, Y. Yuan, D. Luo, K. Feng, R. S. Yassar, X. Wang, Z. Chen, J. Lu, A lithium–sulfur battery using a 2D current collector architecture with a large-sized sulfur host operated under high areal loading and low E/S ratio. *Adv. Mater.* **30**, 1804271 (2018).
30. S.-H. Chung, A. Manthiram, Lithium–sulfur batteries with superior cycle stability by employing porous current collectors. *Electrochim. Acta* **107**, 569–576 (2013).
31. L.-J. Liu, Y. Chen, Z. F. Zhang, X. L. You, M. D. Walle, Y. J. Li, Y. N. Liu, Electrochemical reaction of sulfur cathodes with Ni foam current collector in Li-S batteries. *J. Power Sources* **325**, 301–305 (2016).
32. N. Liu, G. Zhou, A. Yang, X. Yu, F. Shi, J. Sun, J. Zhang, B. Liu, C.-L. Wu, X. Tao, Y. Sun, Y. Cui, S. Chu, Direct electrochemical generation of supercooled sulfur microdroplets well below their melting temperature. *Proc. Natl. Acad. Sci. U.S.A.* **116**, 765–770 (2019).
33. G. M. Zhou, D.-W. Wang, F. Li, P.-X. Hou, L. Yin, C. Liu, G. Q. Lu, I. R. Gentle, H.-M. Cheng, A flexible nanostructured sulphur–carbon nanotube cathode with high rate performance for Li-S batteries. *Energ. Environ. Sci.* **5**, 8901–8906 (2012).
34. G. M. Zhou, S. Pei, L. Li, D.-W. Wang, S. Wang, K. Huang, L.-C. Yin, F. Li, H.-M. Cheng, A graphene–pure-sulfur sandwich structure for ultrafast, long-life lithium–sulfur batteries. *Adv. Mater.* **26**, 625–631 (2014).
35. Y. Diao, K. Xie, S. Xiong, X. Hong, Insights into Li-S battery cathode capacity fading mechanisms: Irreversible oxidation of active mass during cycling. *J. Electrochem. Soc.* **159**, A1816–A1821 (2012).
36. D. Aurbach, E. Pollak, R. Elazari, G. Salitra, C. S. Kelley, J. Affinito, On the surface chemical aspects of very high energy density, rechargeable Li-Sulfur batteries. *J. Electrochem. Soc.* **156**, A694–A702 (2009).
37. J. Xiao, L. Wan, S. Yang, F. Xiao, S. Wang, Design hierarchical electrodes with highly conductive $NiCo_2S_4$ nanotube arrays grown on carbon fiber paper for high-performance pseudocapacitors. *Nano Lett.* **14**, 831–838 (2014).
38. Z. P. Chen, W. Ren, L. Gao, B. Liu, S. Pei, H.-M. Cheng, Three-dimensional flexible and conductive interconnected graphene networks grown by chemical vapour deposition. *Nat. Mater.* **10**, 424–428 (2011).
39. D. Voiry, J. Yang, J. Kupferberg, R. Fullon, C. Lee, H. Y. Jeong, H. S. Shin, M. Chhowalla, High-quality graphene via microwave reduction of solution-exfoliated graphene oxide. *Science* **353**, 1413–1416 (2016).
40. A. C. Ferrari, J. Robertson, Interpretation of Raman spectra of disordered and amorphous carbon. *Phys. Rev. B* **61**, 14095–14107 (2000).
41. A. Yang, G. Zhou, X. Kong, R. A. Vilá, A. Pei, Y. Wu, X. Yu, X. Zheng, C.-L. Wu, B. Liu, H. Chen, Y. Xu, D. Chen, Y. Li, S. Fakra, H. Y. Hwang, J. Qin, S. Chu, Y. Cui, Electrochemical generation of liquid and solid sulfur on two-dimensional layered materials with distinct areal capacities. *Nat. Nanotech.* **15**, 231–237 (2020).
42. G. M. Zhou, L. Li, C. Ma, S. Wang, Y. Shi, N. Koratkar, W. Ren, F. Li, H.-M. Cheng, A graphene foam electrode with High sulfur loading for flexible and High energy Li-S batteries. *Nano Energy* **11**, 356–365 (2015).
43. F. Wu, Y.-S. Ye, J.-Q. Huang, T. Zhao, J. Qian, Y.-Y. Zhao, L. Li, L. Wei, R. Luo, Y.-X. Huang, Y. Xing, R.-J. Chen, Sulfur nanodots stitched in 2D "Bubble-Like" interconnected carbon fabric as reversibility-enhanced cathodes for lithium–sulfur batteries. *ACS Nano* **11**, 4694–4702 (2017).
44. G. Gao, Y. Jiao, E. R. Waclawik, A. Du, Single Atom (Pd/Pt) supported on graphitic carbon nitride as an efficient photocatalyst for visible-light reduction of carbon dioxide. *J. Am. Chem. Soc.* **138**, 6292–6297 (2016).
45. G. Kresse, J. Furthmüller, Efficient iterative schemes for ab initio total-energy calculations using a plane-wave basis set. *Phys. Rev. B Condens. Matter.* **54**, 11169–11186 (1996).
46. G. Kresse, J. Furthmüller, Efficiency of ab-initio total energy calculations for metals and semiconductors using a plane-wave basis set. *Comput. Mater. Sci.* **6**, 15–50 (1996).
47. J. P. Perdew, K. Burke, M. Ernzerhof, Generalized gradient approximation made simple. *Phys. Rev. Lett.* **77**, 3865–3868 (1996).
48. S. Grimme, Semiempirical GGA-type density functional constructed with a long-range dispersion correction. *J. Comput. Chem.* **27**, 1787–1799 (2006).
49. G. Henkelman, B. P. Uberuaga, H. Jónsson, A climbing image nudged elastic band method for finding saddle points and minimum energy paths. *J. Chem. Phys.* **113**, 9901–9904 (2000).

Acknowledgments

Funding: Y.C. acknowledges the support from the Assistant Secretary for Energy Efficiency and Renewable Energy, Office of Vehicle Technologies of the U.S. Department of Energy under the Battery Materials Research (BMR) Program and the Battery500 Consortium. G.Z. was supported by the Natural Key Research and Development Program of China (number 2019YFA0705700). Part of this work was performed at the Stanford Nano Shared Facilities and the Stanford Nanofabrication Facility. **Author contributions:** G.Z. and Y.C. conceived the concept and experiments. G.Z., A.Y., and X.Y. designed and built the in situ cells and carried out imaging and electrochemical measurements. G.G. and L.-W.W. carried out the DFT calculations. J.X. and C.L. assisted in material preparation. Y.Y., A.P., Y.W., Y.P., Y.L., Z.L., and K.L. assisted in the device fabrication and electrochemical measurements. G.Z., A.Y., G.G., J.X., and Y.C. analyzed data and wrote the paper. All authors discussed the results and commented on the manuscript. **Competing interests:** The authors declare that they have no competing interests. **Data and materials availability:** Readers are welcome to comment on the online version of the paper. All data needed to evaluate the conclusions in the paper are present in the paper and/or the Supplementary Materials. Additional data related to this paper may be requested from the authors.

Submitted 25 June 2019
Accepted 16 March 2020
Published 22 May 2020
10.1126/sciadv.aay5098

Citation: G. Zhou, A. Yang, G. Gao, X. Yu, J. Xu, C. Liu, Y. Ye, A. Pei, Y. Wu, Y. Peng, Y. Li, Z. Liang, K. Liu, L.-W. Wang, Y. Cui, Supercooled liquid sulfur maintained in three-dimensional current collector for high-performance Li-S batteries. *Sci. Adv.* **6**, eaay5098 (2020).